ELSEVIER

Physica E 15 (2002) 131–152

PHYSICA E

www.elsevier.com/locate/physe

Self-assembled (In,Ga)As/GaAs quantum-dot nanostructures: strain distribution and electronic structure

Valeria-Gabriela Stoleru[a,*], Debdas Pal[b], Elias Towe[b]

[a] *Laboratory for Optics and Quantum Electronics, Department of Electrical and Computer Engineering, University of Virginia, Charlottesville, VA 22904-4743, USA*

[b] *Laboratory for Photonics, Department of Electrical and Computer Engineering, Carnegie Mellon University, Pittsburgh, PA 15213, USA*

Received 30 October 2001; accepted 13 March 2002

Abstract

This paper presents a simple analytical method for calculating the strain distribution in and around self-assembled (In,Ga)As/GaAs quantum-dot nanostructures. The dots are assumed to be buried in an infinite medium so that the effects of free surfaces can be neglected. This assumption is based on the relative size of the dot, compared to that of the overlayer. The model—based on classical continuum elasticity—is capable of handling dots of arbitrary shapes; here, however, only dots with pyramidal and truncated-pyramidal shapes are considered. The approximate shape of the dots is extracted from high-resolution transmission electron microscope observations. The electronic energy levels in the dots are calculated by solving the three-dimensional effective mass Schrödinger equation. The carrier confinement potential in this equation is modified by the strain distribution. Because the dots are in a strong confinement regime, the effects of Coulomb interactions are neglected. The calculated confined eigen-energies agree with our experimental photoluminescence data. The calculations also support previous results reported by others.

PACS: 83.85.St; 73.21.La; 68.66.Hb; 68.37.Lp; 73.43.Cd

Keywords: Quantum dots; Strain; Eight-band model; Electronic spectra; Nanostructures

1. Introduction

Progress in nanotechnology has resulted in the synthesis of nanometer-scale self-assembled quantum dots for potential applications in electronics and optoelectronics. Several devices that include quantum dots in their active regions have been proposed in the past few years; some of them, such as lasers, infrared detectors, and memory elements have been demonstrated. Since millions of dots are generally required to yield macroscopic effects, a narrow-size distribution is important for optimum device performance. The synthesis of uniform-sized dots is still a research problem and much remains to be learned in understanding the growth processes that lead to pristine and uniform-sized quantum dots. The most studied quantum-dot system today is based on the spontaneous formation of (In,Ga)As islands on a GaAs substrate during heteroepitaxy. This process is a consequence of the strain which results from the in-plane lattice-mismatch between the (In,Ga)As and the GaAs. The specific shape of the dots is usually

* Corresponding author.

E-mail addresses: gstoleru@virginia.edu (V.-G. Stoleru), towe@cmu.edu (E. Towe).

1386-9477/02/$ - see front matter
PII: S1386-9477(02)00459-9

a function of the growth parameters and the general environment of the dots. Some researchers have observed dots with hemispherical shapes; others have observed dot-shapes that are multifaceted domes; and yet several other groups have reported dots with pyramidal shapes [1]. It is generally difficult to determine the shape of the dots in situ during growth; the lateral extent and height of the dots, however, can often be determined approximately for surface quantum dots from atomic force microscope studies. Better estimates of buried dot-sizes can usually be obtained from transmission electron microscope studies; these studies can generally provide valuable information about the shape of the dots [2]. Central to understanding many properties of the dot is a need to determine the elastic strain distribution in and around the dots. The strain distribution profoundly affects the electronic structure, and hence the optical properties of the dots by modifying the energies and wave functions for confined carriers. The principal aim of this paper is to quantitatively determine the stress fields and hence the strain distribution in and around a dot. This information is then used to calculate the electronic structure of the dots.

Strain drives the Stranski–Krastanow growth process that leads to the formation of dots; residual strain, in general, can have interesting effects on the electronic and optical properties of semiconductor structures. The effects of strain on semiconductors have therefore motivated a significant interest in calculating its magnitudes in a broad range of devices [3]. The hydrostatic (ε_h) component of strain, for example, usually shifts the conduction and valence band-edges of semiconductors; biaxial (ε_b) strain, on the other hand, modifies the valence bands by splitting the degeneracy of the light- and heavy-hole bands. These effects have a profound impact on the electronic and optical properties of the structures out of which devices might be fabricated.

The two general classes of techniques used in the calculation of strain include the finite difference [4,5] and atomistic calculation methods [6]. Both of these methods require considerable computational resources. In the atomistic approach, there is an implicit reliance on the validity of the valence force field model with a Keating interatomic potential. This method, however, has recently been shown to be questionable for small islands whose base dimensions are smaller than 10 nm [7]; for these islands, the Stillinger–Weber potential has been suggested as an alternative potential. The finite element and finite difference methods have been used by several groups [4,8–11]. One advantage of the finite element and finite difference methods is that they can be used to treat problems with complex geometries. This advantage, however, is offset by the demand on computational resources. Another variant of these methods is the boundary element approach; this, however, can be mathematically complex [12]. A simple and elegant method for calculating strain fields around a single, isotropic, cubic dot has been presented by Downes et al. [13]. This method is based on a simplification of Eshelby's classic inclusion theory [14]. The method first identifies a set of vectors such that the divergence of each gives the Green's function for the stress components σ_{ij}. By invoking Gauss' theorem, the stress field is determined by performing an integral over the surface of the dot.

In this paper, we extend the method to more complex and practical geometries. We particularly focus on regular pyramids and those with truncated tops. In the model, we make the basic assumption that the elastic properties of the materials are isotropic [15]. This assumption does not seriously affect any qualitative conclusions drawn from the calculations. In any event, it has been shown in a recent paper [16] that as long as the symmetry of the shape of the structure is less than or equal to the cubic symmetry of the crystal, both anisotropic and isotropic models give similar results. We caution however that even though this is true for quantum-dot nanostructures, it is not so for quantum-well heterostructures.

Our calculations here are for the (In,Ga)As/GaAs materials system. The model, however, is general enough that it can be used for similar other materials systems. For the InAs/GaAs system, the initial strain or lattice-mismatch is defined as $\varepsilon_0 = (a_{GaAs} - a_{InAs})/a_{InAs} = -0.067$. This is the fractional change of the difference between the in-plane lattice constant of the GaAs substrate and the InAs epilayer with respect to the InAs lattice constant; when Ga is included in the composition of the epilayer, the mismatch (strain) becomes $\varepsilon_0 = (a_{GaAs} - a_{In_xGa_{1-x}As})/a_{In_xGa_{1-x}As}$. The Poisson ratios for the binary materials are taken to be 0.316 for the GaAs and 0.354 for the InAs. As is usual in continuum elasticity, we assume that the

materials are continuous, linear, isotropic, and obey Hooke's law. The use of continuum elasticity methods has been experimentally verified to be valid for layers as thin as three atomic monolayers [17]; furthermore, it is estimated theoretically that the method remains valid for layers whose thicknesses are on the order of five atoms [18]. We want to point out that the sensitivity of some physical properties to strain could make anisotropic effects important; the isotropic approximation should therefore be treated with caution, particularly for layers oriented in certain crystallographic directions. For most cases, however, the anisotropy only modifies the strain distributions slightly [16,19].

Classical elasticity and atomistic methods have been shown to give similar results for small strains [20]. Differences become apparent for strains larger than 5%, particularly in the case of semiconductor quantum dots. Even though atomistic elasticity is expected to continue to give reliable results for large strains, the number of atoms involved in the computations makes the method unwieldy for rapid, order-of-magnitude calculations. The advantage of the approach based on Eshelby's inclusion theory is that it is simple and allows one to find approximate analytical expressions for the strain tensor components. As we will show later, for quantum dots with lateral dimensions in the range of 10–20 nm, the strain profiles calculated within the modified Eshelby framework are in good agreement with those obtained by the methods of atomistic elasticity.

This paper is organized as follows: in Section 2 we give a detailed description of the basic model for calculating the strain tensor for pyramidal and truncated pyramidal quantum dots. The strain fields are presented and discussed in Section 3. The method discussed here is a suitable precursor for the calculation of electronic structure based on the envelope function method within the plane-wave expansion technique. One can determine, for example, the strain-dependent matrix element linking any pair of plane waves. We present and discuss the strain-dependent confining potentials for electrons and holes, as well as the electronic energy levels in Section 4. A summary of our results is given in Section 5.

In our calculations, we consider a single isolated dot to facilitate comparison with published results. The dot is assumed to be buried deep within a matrix material. Figs. 1(a) and (b) show the schematic cross-sections of the pyramidal and truncated pyramidal quantum-dot structures under consideration. They are assumed to be on top of a semi-infinite (0 0 1) GaAs substrate on which is grown a thin InAs wetting layer first.

2. Model description

Most theoretical calculations of the properties of InAs dots assume a square-based pyramidal shape [4,6,21]. Here, for purposes of comparison with previously published work, we also consider this geometry. However, we extend our calculations to include the truncated pyramidal case. When a capping layer—for example GaAs—is grown on top of a layer of dots, the morphology of the overlayer is affected by the interaction of the inhomogeneous strain around the dots and in the wetting layer. This affects the apex of the dots. There is then a thermodynamically favored tendency for the adatoms to migrate to the side of the dots [22], resulting in a reduction of the dot height and formation of a flat (0 0 1) top surface.

Following Downes et al. [13], the Lamé potential u during relaxation can be described by a scalar potential

$$u = \frac{1}{2G}\nabla\Phi, \tag{1}$$

where G is the shear modulus, defined as $2G = E/(1+v)$ in Ref. [23]. The displacement potential obeys the Poisson equation

$$\nabla^2\Phi(r) = \frac{1+v}{1-v}\,\varepsilon_0(r)2G. \tag{2}$$

From Eq. (2), a solution can be reached by integration, using Green's function, thus

$$\frac{1}{2G}\,\Phi(r) = -\frac{(1+v)}{(1-v)}\iiint_V \frac{\varepsilon_0(r_0)}{4\pi|r-r_0|}\,\mathrm{d}^3r_0. \tag{3}$$

In the equation above, the function $1/|r-r_0|$ can be written as

$$-\frac{1}{2}\vec{\nabla}\cdot\frac{(r-r_0)}{|r-r_0|}.$$

The point r_0 is within the volume of the dot. The volume integral in Eq. (3) can be converted to a surface integral by applying the divergence theorem to it, with

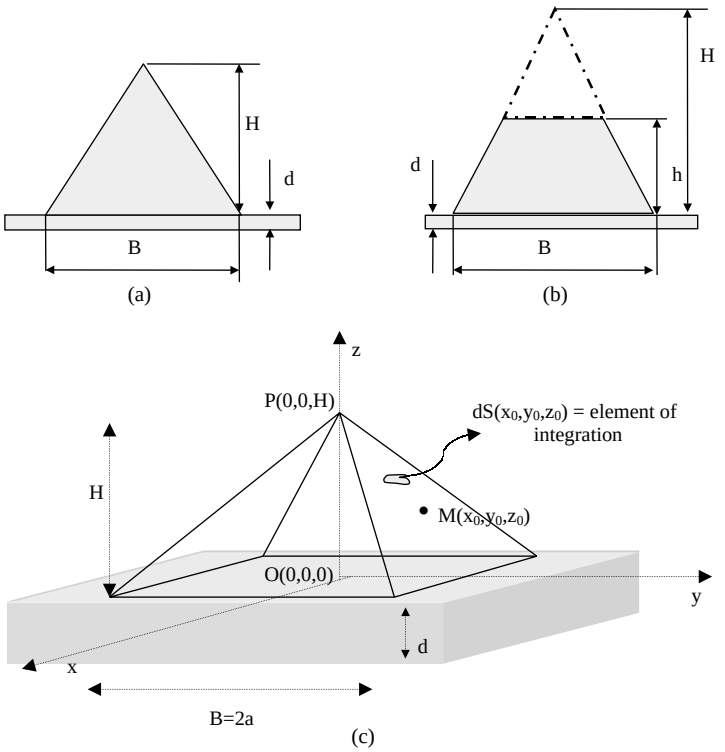

Fig. 1. Schematic models for the pyramidal (a) and truncated pyramidal (b) quantum-dot structures; B = base width, H = pyramid height, t = truncation factor, h = truncated pyramid height, d = thickness of wetting layer; (c) Three-dimensional model of a quantum dot in the Cartesian coordinate system.

the point r_0 now being on the surface of the dot, as shown in Fig. 1(c). Thus

$$\frac{1}{2G}\,\Phi(r) = \frac{1}{8\pi}\,\frac{(1+\nu)}{(1-\nu)} \times \iiint_V \varepsilon_0(r_0)\vec{\nabla}\cdot\frac{(r-r_0)}{|r-r_0|}\,\mathrm{d}^3 r_0 = \frac{1}{8\pi}\,\frac{(1+\nu)}{(1-\nu)} \times \iint_S \varepsilon_0(r_0)\,\frac{(r-r_0)}{|r-r_0|}\,\mathrm{d}S(r_0). \quad (4)$$

The initial lattice-mismatch, ε_0, can be considered constant within the volume of the dot. With the appropriate substitutions, Eq. (1) becomes

$$u = \frac{1}{2G}\,\nabla\Phi = \frac{\varepsilon_0}{4\pi}\,\frac{(1+\nu)}{(1-\nu)}\iint_S \frac{1}{|r-r_0|}\,\mathrm{d}S(r_0). \quad (5)$$

The stress components can therefore be written as

$$\sigma_{ij}(r) = -\frac{\varepsilon_0 E}{8\pi(1-\nu)} \times \iint_S \frac{(i-i_0)\hat{\boldsymbol{i}} + (j-j_0)\hat{\boldsymbol{j}}}{|r-r_0|^3}\,\mathrm{d}S(r_0) + \delta_{ij}\,\frac{E\varepsilon_0}{1-\nu}\iiint_V \delta(r-r_0)\,\mathrm{d}V(r_0), \quad (6)$$

where $\hat{\boldsymbol{i}}$ and $\hat{\boldsymbol{j}}$ are unit vectors in the ith and jth directions, respectively, for $i = x, y, z$, $j = x, y, z$ and $r^2 = x^2 + y^2 + z^2$. The parameter ε_0 is the isotropic misfit strain, E is the Young's modulus, ν is Poisson's ratio, and δ_{ij} is the Kronecker delta function. The last part of Eq. (6) comes from evaluating the limit of the surface integral, as a field point r approaches the boundary point r_0 on the surface of the dot. The misfit strain is taken as negative for a material under compression.

The volume of a square-based, truncated pyramid is defined by

$$-B\frac{(H-z)}{2H} \leqslant x \leqslant B\frac{(H-z)}{2H},$$
$$-B\frac{(H-z)}{2H} \leqslant y \leqslant B\frac{(H-z)}{2H},$$
$$0 \leqslant z \leqslant Ht, \tag{7}$$

where H is the height of the pyramid in the absence of truncation, B is the base of the pyramid, and $0 \leqslant t \leqslant 1$, where t represents the truncation factor. The z-axis is the [0 0 1] growth direction, and the origin of the coordinates is at the center of the square base of the pyramid (the $z = 0$ plane).

After converting to Cartesian coordinates, the integrations indicated in Eq. (6) can be easily carried out. The in-plane stress components have cumbersome mathematical expressions; however, for some particular directions, they can be simplified. For example, for a square-based pyramidal dot, with a contrast ratio (defined as the ratio of the height to the base) of 1:2, where $B = 2a$ and $H = a$, one obtains the following expressions as functions of z:

$$\begin{aligned}\sigma'_{xx} &= \sigma'_{yy} \\ &= 2\left[-\tan^{-1}\left(\frac{z-a}{|z-a|}\right) + \tan^{-1}\left(\frac{z}{\sqrt{2a^2+z^2}}\right)\right] \\ &\quad + \frac{1}{2}\left[\ln\left|\frac{\sqrt{2a^2+z^2}-a}{\sqrt{2a^2+z^2}+a}\right| - \ln\left|\frac{\sqrt{2a^2+z^2}+a}{\sqrt{2a^2+z^2}-a}\right|\right] \\ &\quad + \frac{2}{\sqrt{3}}\left[\ln\left(\frac{-(z-a)}{\sqrt{3}} + |z-a|\right) - \ln\left(\frac{-2a-z}{\sqrt{3}} + \sqrt{2a^2+z^2}\right)\right],\end{aligned} \tag{8}$$

and

$$\begin{aligned}\sigma'_{zz} &= 4\pi - 4\left[-\tan^{-1}\left(\frac{z-a}{|z-a|}\right) + \tan^{-1}\left(\frac{z}{\sqrt{2a^2+z^2}}\right)\right] \\ &\quad + \left[\ln\left|\frac{\sqrt{2a^2+z^2}-a}{\sqrt{2a^2+z^2}+a}\right| - \ln\left|\frac{\sqrt{2a^2+z^2}+a}{\sqrt{2a^2+z^2}-a}\right|\right] \\ &\quad + \frac{4}{\sqrt{3}}\left[\ln\left(\frac{-(z-a)}{\sqrt{3}} + |z-a|\right) - \ln\left(\frac{-2a-z}{\sqrt{3}} + \sqrt{2a^2+z^2}\right)\right].\end{aligned} \tag{9}$$

Note that $\sigma_{ij} = E\varepsilon_0/(4\pi(1-\nu))\sigma'_{ij}$, where ε_0, ν, and E are as defined before. The more general analytical expressions for calculating stress distributions in structures with arbitrary degrees of truncation are given in the Appendix A. The expressions for the strain components follow by substitution of the stress components into Hooke's law. The generalized stress–strain relations are:

$$\sigma_{kl} = C_{klmn}\varepsilon_{mn}, \tag{10}$$

and

$$\varepsilon_{kl} = S_{klmn}\sigma_{mn}, \tag{11}$$

where the C_{klmn} are the compliance and the S_{klmn} the stiffness coefficients. For materials with cubic symmetry, only three of the 81 components are independent. So $C_{11} = C_{1111} = C_{2222} = C_{3333}, C_{12} = C_{1122} = C_{2233}$, etc., and $C_{44} = C_{1212} = C_{2323}$, etc.; similar relations hold for S_{11}, S_{12} and S_{44}. The stress–strain relations can then be written in terms of Young's modulus E and Poisson ratio ν. Since

$$E = \frac{1}{S_{11}} = \frac{(C_{11}-C_{12})(C_{11}+2C_{12})}{C_{11}+C_{12}}, \tag{12}$$

and

$$\nu = -ES_{12} = \frac{C_{12}}{C_{11}+C_{12}}, \tag{13}$$

then

$$\sigma_{ij} = \frac{E}{1+\nu}\varepsilon_{ij} + \frac{\nu E}{(1+\nu)(1-2\nu)}\delta_{ij}\varepsilon_{kk}, \tag{14}$$

and

$$\varepsilon_{ij} = \frac{1}{E}\left[(1+\nu)\sigma_{ij} - \delta_{ij}\nu\sigma_{kk}\right]. \quad (15)$$

In this paper we define the hydrostatic and the biaxial strains as

$$\varepsilon_{\mathrm{h}} = \varepsilon_{xx} + \varepsilon_{yy} + \varepsilon_{zz}, \quad (16)$$

and

$$\varepsilon_{\mathrm{b}} = \varepsilon_{zz} - \tfrac{1}{2}(\varepsilon_{xx} + \varepsilon_{yy}), \quad (17)$$

respectively. These relations are introduced here because they represent important quantities used in the analysis of the electronic energy levels in a later section.

3. Strain distribution

We have calculated the strain distributions for a number of structures whose dimensions are given in Table 1. Calculations for pyramidal QDs, labeled PQD in Table 1, as well as truncated pyramidal dots, labeled TPQD in Table 1, have been carried out. We consider first structure PQD3 in Table 1; this type of structure has been extensively studied and reported on in the literature. Fig. 2 shows the strain tensor components ε_{xx} and ε_{zz} for structure PQD3, plotted as functions of position along the z-axis. The shear strain components, ε_{xy}, ε_{yz}, and ε_{xz} are negligible in the dot and barrier materials; they could, however, be appreciable at the interfaces [4]. By symmetry, the component $\varepsilon_{xx} = \varepsilon_{yy}$. In a thin substrate region below the dot, the GaAs lattice experiences a tensile (positive ε_{xx}) strain in the x–y plane and a compressive (negative ε_{zz}) strain in the z direction. In this case, the dot is forcing the substrate lattice constant to be that of InAs ($a_{\mathrm{InAs}} = 6.05$ Å). In the base region of the dot, the situation is reversed. Here, ε_{zz} is positive and ε_{xx} negative because the substrate now attempts to force the dot lattice constant to be that of GaAs ($a_{\mathrm{GaAs}} = 5.65$ Å). With increasing height within the dot, ε_{zz} changes its sign, becoming negative at the top of the pyramid. At the top of the pyramid, the dominant forces acting on the dot originate from the GaAs matrix at the sides, causing a compressive strain (negative ε_{zz}) along the z direction and a tensile strain (positive ε_{xx}) in the x–y plane. Fig. 3 is a plot of the ε_{xx} and ε_{zz} components along the x-axis for structure PQD3. Within the dot, both ε_{xx} and ε_{zz} are negative, implying the existence of a region of hydrostatic compression. The ε_{xx}, ε_{yy}, and ε_{zz} components of the strain tensor are plotted in Figs. 4(a), (b), and (c) in the x–z plane.

The hydrostatic and biaxial components of the strain for structure PQD3 are plotted as functions of position along the z-axis in Fig. 5. The hydrostatic strain is compressive within the dot and in the surrounding barrier material. The interior of the quantum dot exhibits a nearly homogeneous hydrostatic strain, while the barrier experiences a small hydrostatic strain. This is because GaAs is stiffer than InAs. The biaxial strain tends to be negative in the barrier and positive in the dot, and it is zero near the center of the dot. In this region, the strain is entirely hydrostatic in character. Fig. 5 suggests that a significant transfer of biaxial strain to the barrier takes place.

Table 1
Dimensions of single (In,Ga)As/GaAs quantum-dot structures used for computations

Structure	Base width B (nm)	Pyramid height H (nm)	Truncation factor t	Truncated pyramid height h (nm)
PQD1	12	3		
PQD2	12	4		
PQD3	12	6		
PQD4	16	6		
PQD5	20	6		
TPQD1	13.8	4.6	0.25	1.15
TPQD2	13.8	4.6	0.50	2.30
TPQD3	13.8	4.6	0.75	3.45
TPQD4	19.7	4.7	0.64	3.00

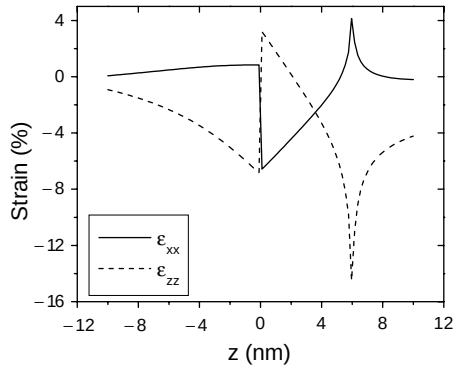

Fig. 2. Strain tensor components ε_{xx} and ε_{zz} for structure PQD3 plotted along the z-axis.

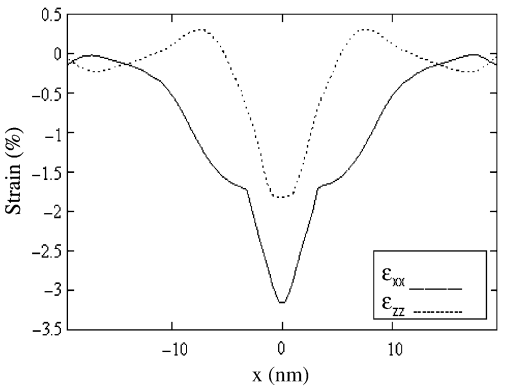

Fig. 3. Strain tensor components ε_{xx} and ε_{zz} for structure PQD3 plotted along the x-axis.

We have studied strain relaxation in the pyramidal InAs/GaAs QDs for the different structures labeled PQD(1–5) in Table 1. We compare the strain distributions in the x–z plane for dots of different base widths ($B_1 = 12$ nm for PQD3, $B_2 = 16$ nm for PQD4, and $B_3 = 20$ nm for PQD5) but the same height ($H = 6$ nm) in Fig. 6. We note that for dots with small base widths, the strain components change sign from the base region of the dot to the apex more rapidly than for dots with large base widths. For example, in structure PQD5, the strain components ε_{xx} and ε_{yy} are negative inside the dot, while in structure PQD3, they change sign from negative at the base of the dot to positive at the apex of the dot. The strain component ε_{zz} changes rapidly from positive to negative values along the

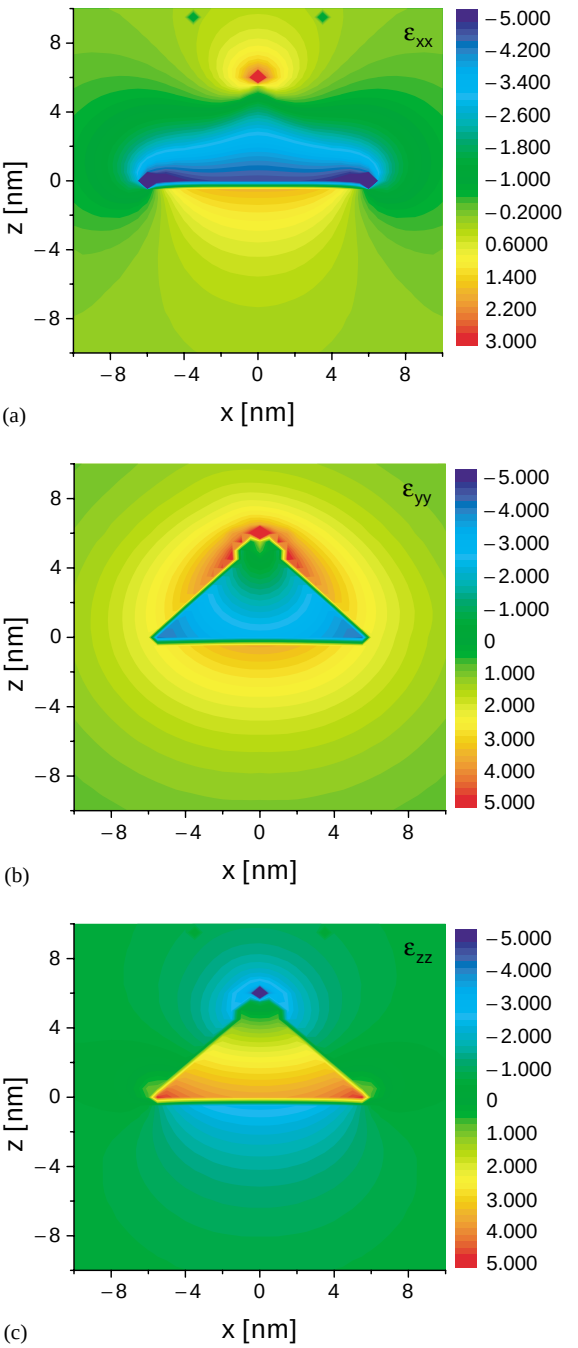

Fig. 4. Strain tensor components for structure PQD3 in the x–z plane: (a) ε_{xx}, (b) ε_{yy}, (c) ε_{zz} (strain expressed in %).

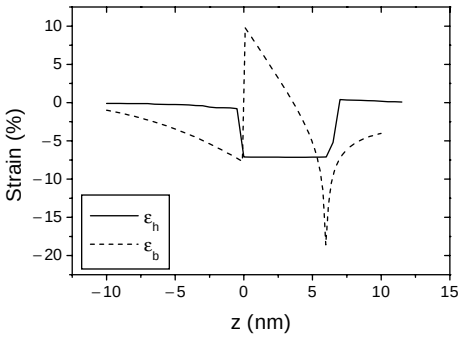

Fig. 5. The hydrostatic ε_h, and biaxial ε_b components of the strain for structure PQD3 plotted along the z-axis.

z-axis in structure PQD3, but is mostly tensile inside structure PQD5. The electronic structure of the dots is also expected to have such a strong dependence on the base lengths, as we will discuss in Section 4.

Fig. 7 illustrates the strain relaxation pattern for InAs dots of the same base width ($B = 12$ nm) but different heights ($H_1 = 3$ nm for PQD1, $H_2 = 4$ nm for PQD2, and $H_3 = 6$ nm for PQD3). This comparison suggests that the strain-modified electronic energy structure is likely not to be as sensitive to variations in the height of the dot as it is to changes in the base width of the dot. Extraordinarily tall dots have large hydrostatic strains near their centers. This increases the band gap inside the islands, partially compensating for the change in confinement potential.

Calculations indicate that when InAs self-assembled pyramidal dots are buried under a GaAs overlayer, significant tensile stress is induced at the top of the dot; the stress at the edges of the dot, on the other hand, is weak and compressive. This is in contrast to surface dots, where stress relaxation occurs at the island tops but is concentrated at the edges [10]. It should be noted that the stress component σ_{zz} (at the $x = 0$ plane) is compressive (negative) in embedded dots whereas it is tensile (positive) in uncovered ones. The strain distribution maps calculated here for pyramidal InAs dots are in reasonably good agreement with published results obtained by calculations based on atomistic methods [4,24]. The agreement is surprisingly good considering the computational simplifications introduced in the present work.

We have extended the analytical procedure to calculating strain distributions of truncated InAs pyramidal dots such as that shown in the transmission electron microscope (TEM) image of Fig. 8. The structure in this figure was grown by molecular beam epitaxy on a (0 0 1) GaAs substrate. From the substrate up, the structure consists nominally of a 250-nm-GaAs buffer layer; this is followed by five periods of InAs/GaAs quantum dots. The entire structure is caped with 27 nm of GaAs. The dot density, as determined by atomic force microscope, was about 4×10^{10} cm^{-2}. The shape of the dots was determined from cross-sectional TEM studies. The TEM image clearly shows that the dots are coherent, with no observable dislocations. The dots could be discerned from their darker appearance due to the presence of Indium. The buried dots appear to be pyramids with truncated tops; their base and height were found to be $B = 13.8$ nm, and $h = 3.4$ nm, respectively. This corresponds to a truncation factor of $t = 0.75$ (structure TPQD3 in Table 1). This observation is consistent with previous reports [25]. We have calculated the strain tensor components, as well as the hydrostatic and the biaxial strain profiles for this structure. The results are shown in solid lines in Fig. 9. We mention that the analytical results obtained for structure TPQD3 are in very good agreement with those obtained for a similar structure, using finite element method, in Ref. [26].

For pyramidal dots of arbitrary truncation, general expressions for the stress tensor components can be derived. These expressions are given in the Appendix A for a uniformly lattice-mismatched InAs/GaAs dot. Calculations based on these expressions for truncated InAs/GaAs dots have been performed for structures TPQD(1–3) in Table 1. The specific truncation factors used are $t = 0.25$, 0.50, and 0.75, respectively. For $t = 1$ we obtain the whole pyramidal geometry, while for $t = 0$, we merely reproduce results for the two-dimensional wetting layer alone.

There are several features that are common to all strain distributions for the structures studied. First, the magnitudes of the strain components are largest at the dot/matrix interface, particularly at the vertices. The strain is rapidly attenuated within the dot and in the matrix material immediately below the square base of the dot. It remains of similar form for each truncation since the base of the dot is unchanged. The hydrostatic strain is zero in the matrix material and proportional to ε_0 in the quantum dot, consistent with standard inclusion theory. The conduction band shift

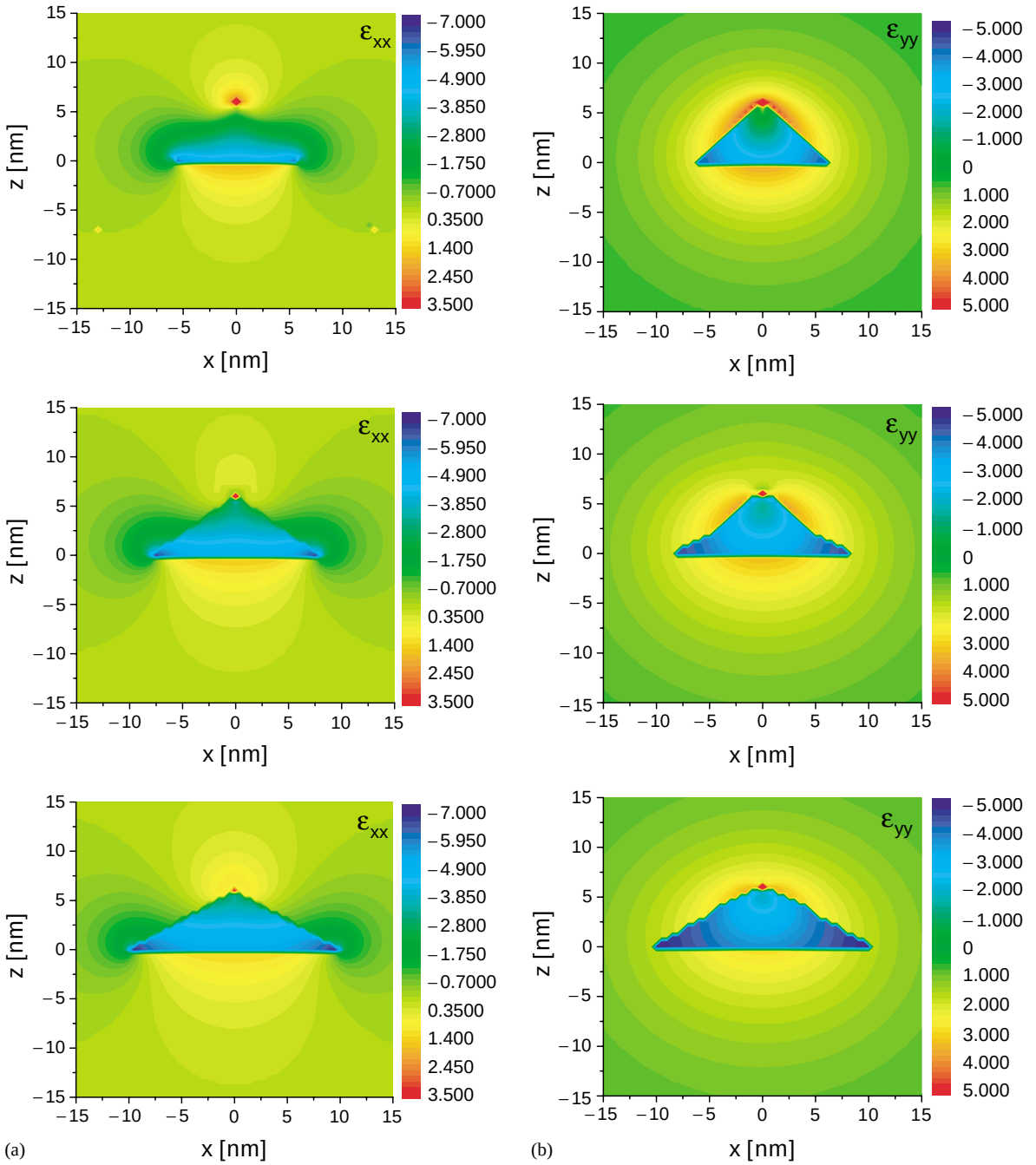

Fig. 6. Comparison of strain components for structures PQD(3-5), characterized by height $H = 6$ nm, but different base widths: $B_1 = 12$ nm (PQD3), $B_2 = 16$ nm (PQD4), and $B_3 = 20$ nm (PQD5): (a) ε_{xx}, (b) ε_{yy}, (c) ε_{zz} (strain expressed in %).

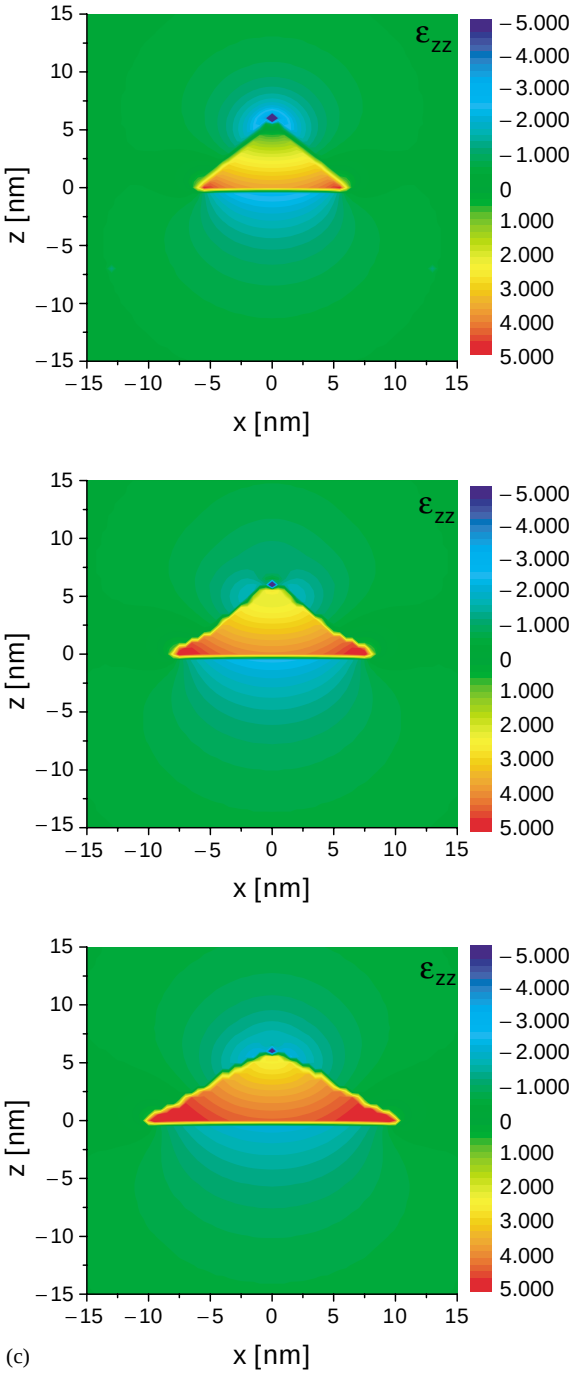

Fig. 6. (*Continued.*)

depends on the hydrostatic strain, so the conduction band shift is relatively constant within a dot of constant composition. Figs. 9(a) and (b) illustrate the ε_{xx} and ε_{zz} strain tensor components plotted along the z-axis for structures TPQD(1–3) of Table 1.

Our results, and those of others, indicate that the magnitudes of the strain components depend on the geometries of the dots. This is as it should be for both qualitative and quantitative reasons. Consider, for example, that the biaxial strain is very sensitive to truncation (see Fig. 9(c)); at the apex of the pyramid, the biaxial strain is negative, but becomes increasingly positive as the degree of truncation increases.

For structure TPQD4 we consider the case where the dot material is a ternary compound; in particular, we consider the case where the Indium composition is 23%, as determined from X-ray diffraction experiments. And as before, the shape and size of the dots are determined from cross-sectional high-resolution TEM observations. We have performed calculations to determine the strain tensor components for $In_{0.23}Ga_{0.77}As/GaAs$ dots. The strain distributions are depicted in Fig. 10 for structure TPQD4. The strain tensor components obtained here are used as input for the electronic band structure calculations discussed in the next section.

4. Electronic structure and optical transitions

The band structure of semiconductors is generally altered by the presence of strain, which changes the lattice constant and reduces the symmetry of the crystal. Strain modifies energy gaps and removes degeneracy. Here, we take account of the strain distributions discussed in the previous sections in calculating the electronic structure of dots in the envelope function approximation using an eight-band strain-dependent $\boldsymbol{k}\cdot\boldsymbol{p}$ Hamiltonian [27]. The eight-band $\boldsymbol{k}\cdot\boldsymbol{p}$ method represents an extension of the Luttinger–Kohn formalism, which describes coupling among the light-hole, heavy-hole and split-off valence bands to second order in $\boldsymbol{k}$, but is modified to include the linear coupling between the conduction and valence band states. This is necessary in order to correctly model conduction band non-parabolicity. A product of strain components and a deformation potential describes the general form of the strain-induced modification of the band

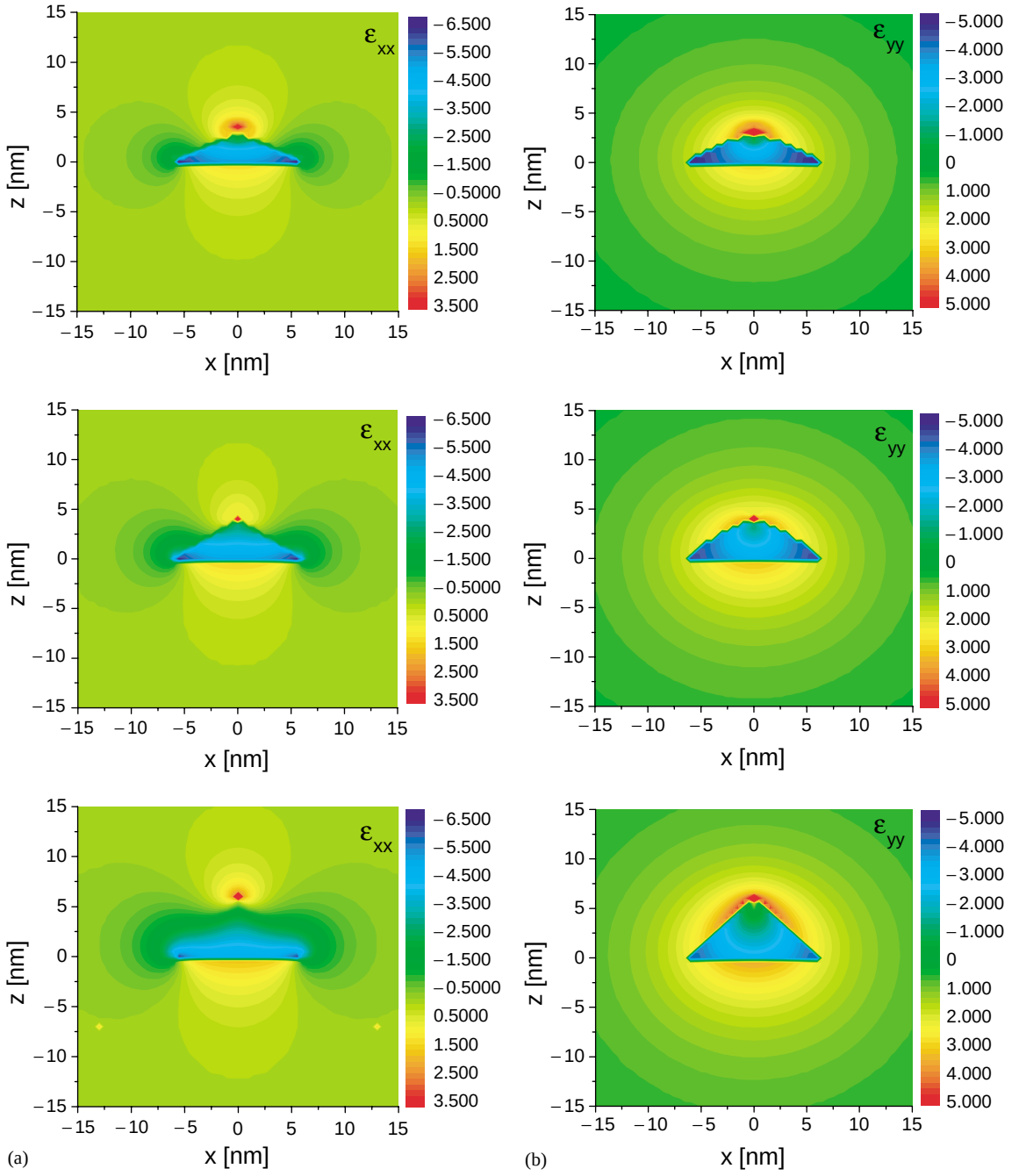

Fig. 7. Comparison of strain components for structures PQD(1–3), characterized by base width $B = 12$ nm, but different heights: $H_1 = 3$ nm (PQD1), $H_2 = 4$ nm (PQD2), and $H_3 = 6$ nm (PQD3): (a) ε_{xx}, (b) ε_{yy}, (c) ε_{zz} (strain expressed in %).

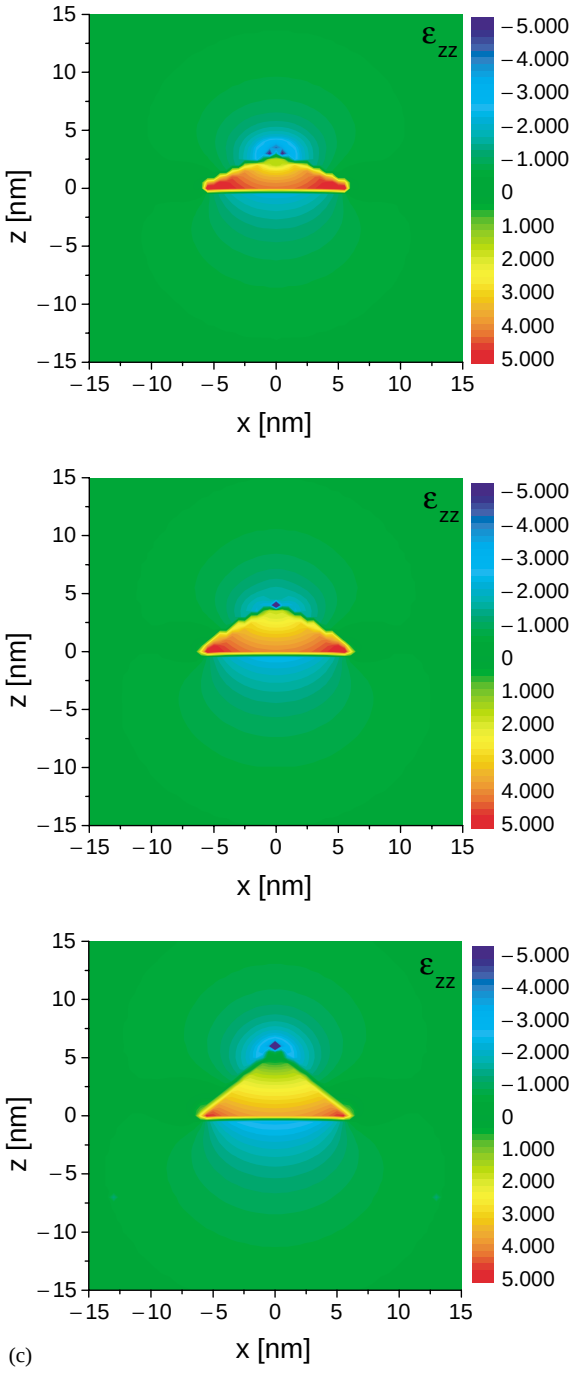

(c)

Fig. 7. (*Continued.*)

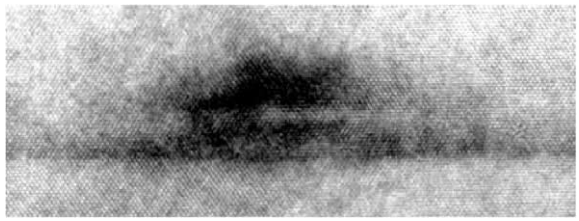

Fig. 8. Cross-sectional high-resolution transmission electron microscope image of InAs quantum dots in a GaAs matrix.

structure. Typical values of deformation potentials range from 1 to 10 eV [22]. These determine the amount of band structure modification and enter the calculations as material parameters given in Table 2. In our calculations, we neglect the lack of inversion symmetry in the zincblende structure and consequently ignore the small coupling of the conduction band to shear deformations. In the strain-dependent Hamiltonian, the non-diagonal terms containing shear components of the strain are non-zero in our geometries, except far away from the dot axis. However, since the diagonal shear strain term of the Hamiltonian decouples the heavy- and light-hole bands by approximately 100 meV, the correction of the non-diagonal terms in the Hamiltonian is small near the band-edge. The resultant Hamiltonian is a matrix that is diagonalized using the Lanczos algorithm developed in Refs. [28,29].

Some insight can be gleaned by examining the strain-induced modification to the band structure corresponding to structure PQD3 in Table 1. In the absence of strain, the confining potential for an electron (hole) is a square well formed by the difference in the absolute energy of the conduction (valence) band-edges in InAs and GaAs [30]. In the conduction band, the depth of the confining potential in this case is about 840 meV. For holes, the potential well is about 263 meV deep. However, because of strain, the confining potential for each carrier type is shifted. Since the strain varies with position, the confining potentials will also vary with position. The material parameters used in our computations are given in Table 2. Under these considerations, the conduction band can be given as

$$E_c(\varepsilon) = E_c^0 + \delta E_c(\varepsilon), \tag{18}$$

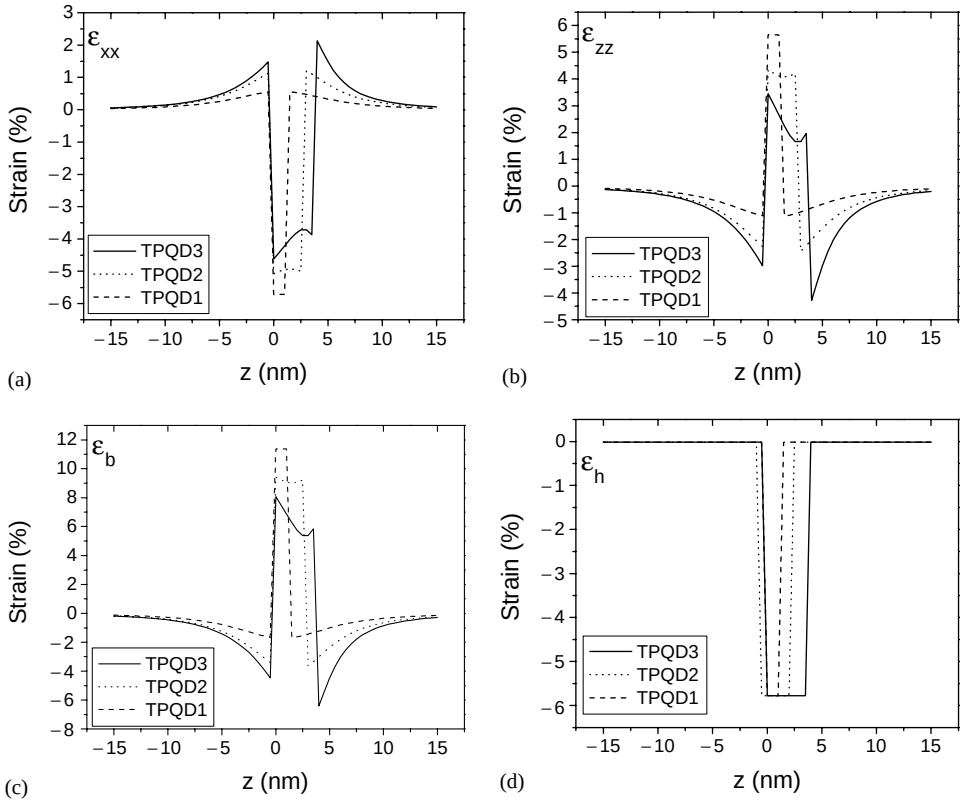

Fig. 9. Strain tensor components ε_{xx} and ε_{zz} along the z-axis for $t = 0.25$ (TPQD1), $t = 0.50$ (TPQD2), and $t = 0.75$ (TPQD3): (a) ε_{xx}, (b) ε_{zz}, (c) ε_{b}, and (d) ε_{h}.

where E_{c}^{0} is the offset of the unstrained conduction band, which is

$$E_{\mathrm{c}}^{0} = E_{\mathrm{v,av}}^{0} + \frac{\Delta_0}{3} + E_{\mathrm{g}}, \tag{19}$$

and δE_{c} is the strain-induced shift of the conduction band which is expressed as

$$\delta E_{\mathrm{c}}(\varepsilon) = a_{\mathrm{c}}(\varepsilon_{xx} + \varepsilon_{yy} + \varepsilon_{zz}). \tag{20}$$

In Eq. (19), Δ_0 is the spin-orbit splitting, E_{g} is the unstrained band gap, and $E_{\mathrm{v,av}}^{0}$ is the unstrained average valence band-edge. The parameter a_{c} in Eq. (20) is the deformation potential for the conduction band.

The effect of strain on the valence band depends largely on the symmetry of the strain. The heavy- and light-hole energy bands, $E_{\mathrm{v}}^{\mathrm{hh}}$ and $E_{\mathrm{v}}^{\mathrm{lh}}$, couple to the individual strain components via the relations [31]:

$$E_{\mathrm{v}}^{\mathrm{hh}} = E_{\mathrm{v,av}}^{0} + \frac{\Delta_0}{3} + \delta E_{\mathrm{v,h}} - \frac{1}{2}\,\delta E_{\mathrm{v,b}}, \tag{21}$$

and

$$E_{\mathrm{v}}^{\mathrm{lh}} = E_{\mathrm{v,av}}^{0} - \frac{\Delta_0}{6} + \delta E_{\mathrm{v,h}} + \frac{1}{4}\,\delta E_{\mathrm{v,b}} + \frac{1}{2}\sqrt{\Delta_0^2 + \Delta_0 \delta E_{\mathrm{v,b}} + \frac{9}{4}(\delta E_{\mathrm{v,b}})^2}, \tag{22}$$

where $\delta E_{\mathrm{v,h}} = a_{\mathrm{v}}\varepsilon_{\mathrm{h}}$, and $\delta E_{\mathrm{v,b}} = b\varepsilon_{\mathrm{b}}$. The deformation potentials a_{v} and b are given in Table 2.

The dominant effect of the strain is that the dot experiences a large increase in its band gap due to the considerable hydrostatic pressure. The conduction band for structure PQD3 in Table 1 has a potential well that is 0.4 eV deep at the base of the dot, tapering off to a depth of about 0.27 eV at the apex. The valence band has a more complicated structure. If we could somehow turn off the strain, the holes would be confined to the InAs by a well that is only 85 meV deep. However, the presence of strain alters this considerably,

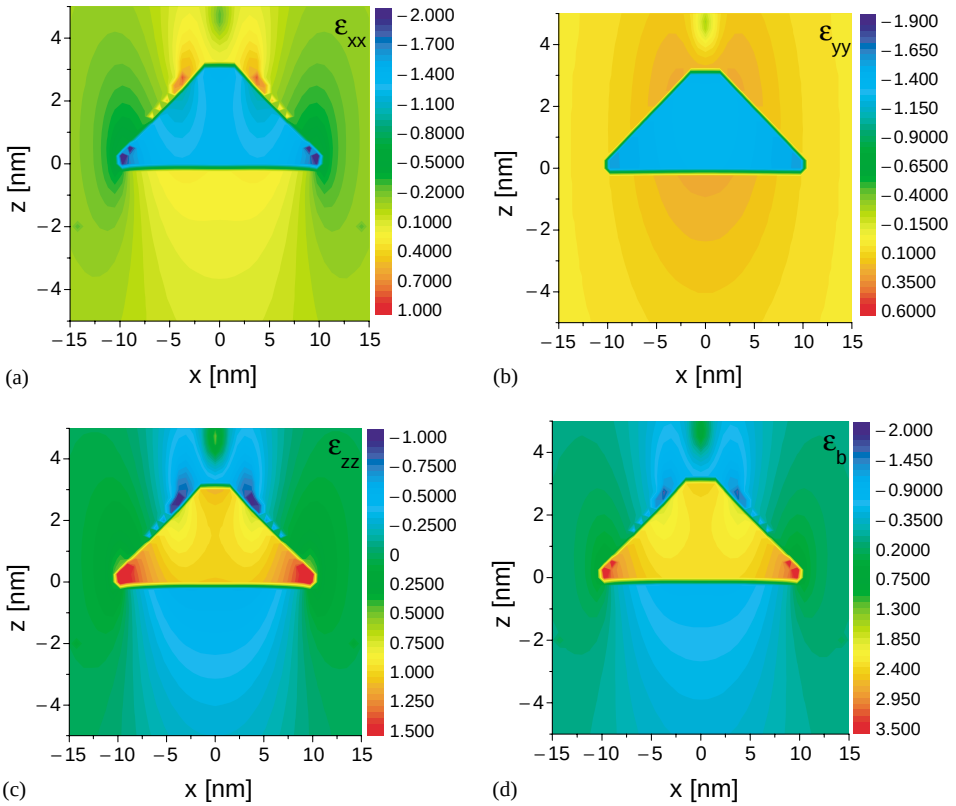

Fig. 10. Strain tensor components in the x–z plane for structure TPQD4: (a) ε_{xx}, (b) ε_{yy}, (c) ε_{zz}, and (d) ε_{b} (strain expressed in %).

Table 2
Material parameters used in calculations

Parameter	GaAs	InAs	$\mathrm{In}_x\mathrm{Ga}_{1-x}\mathrm{As}$
a (Å)	5.6503	6.0553	$(5.6503 + 0.405x)$ [32,39,40]
E_{g} (eV)	1.518	0.413	$(1.518 - 1.580x + 0.475x^2)$ [30,33,39,40] [$T = 6.4$ K]
E_{g} (eV)	1.424	0.324	$[0.324 + 0.7(1-x) + 0.4(1-x)^2]$ [39,40] [$T = 300$ K]
Δ_0 (eV)	0.340	0.380	$(0.340 - 0.093x + 0.133x^2)$ [30,38,39]
C_{11} (N/m^2)	11.88	8.33	$(11.88 - 3.55x)$ [32,33,39,40]
C_{12} (N/m^2)	5.38	4.53	$(5.38 - 0.85x)$ [32,33,39,40]
a_{c} (eV)	−8.013	−5.08	$(-8.013 + 2.933x)$ [30,33,39]
a_{v} (eV)	1.16	1.00	[30,33,39]
b (eV)	−1.7	−1.8	[30,33,39]
$E^0_{\mathrm{v,av}}$ (eV)	−6.92	−6.747	$(-6.92 + 0.231x - 0.058x^2)$ [30,33,39]
m^*_{e}	$0.0667m_0$	$0.02226m_0$	$(0.0667 - 0.0419x - 0.00254x^2)$ [33,39]
E_{p} (eV)	25.7	22.2	$\left[(1.238 - 0.2095x)(1 - m_{\mathrm{e}}/m_{\mathrm{e}})(3E_{\mathrm{g}}(E_{\mathrm{g}} + \Delta_0)/3E_{\mathrm{g}} + 2\Delta_0)\right]$ [33,38]

and it, in fact, makes the dominant contribution to the hole confinement potential. A remarkable feature of the valence band is that it is peaked at the apex of the dot and near the base. This is clearly evident in the energy band diagram presented along the z-axis for structure PQD3 in Fig. 11.

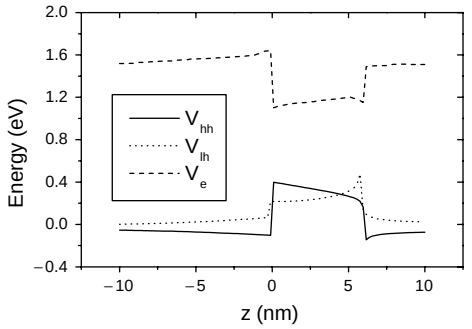

Fig. 11. Electron (V_e), heavy-hole (V_{hh}), and light-hole (V_{lh}) potential profiles for structure PQD3, plotted along the z-axis.

The confining potentials, inclusive of the effects of strain, are piecewise continuous functions of position. These potentials are shown in Fig. 11 for both electrons and holes. The split-off valence band is sufficiently far off in energy from the heavy- and light-hole band-edges, so it plays no role in the calculations. Note that the heavy- and light-hole confining potential wells are shown inverted. The anisotropic (biaxial) components of the strain in the dot and barrier reduce the symmetry of the conventional cubic unit cells, lifting the heavy- and light-hole degeneracy. The compressive strain in the barrier shifts the GaAs conduction band-edge slightly above the unstrained level of 1.52 eV. Note that in Fig. 11, the light-hole band-edge is higher in energy than the heavy-hole band-edge in the barrier, and at the apex of the pyramid. The heavy-hole band is the uppermost band at the base of the pyramid. The direction and magnitude of the splitting of the light- and heavy-hole bands—in the absence of appreciable shear strain components—is dependent solely on the magnitude and sign of the biaxial strain, ε_b. In those regions of the structure where the biaxial strain is negative, the light-hole band will be shifted upwards in energy and the heavy-hole band downwards; in those regions where the biaxial strain is positive, the heavy-hole band will be uppermost. When the biaxial strain is zero, the light- and heavy-hole bands are degenerate.

We show the electron confining potential in the x–z plane in Fig. 12(a) for structure PQD3. Here, the zero of energy is fixed at the GaAs level. The potential well for electrons has a depth of about 400 meV over much of the pyramid, deepening to about 450 meV at

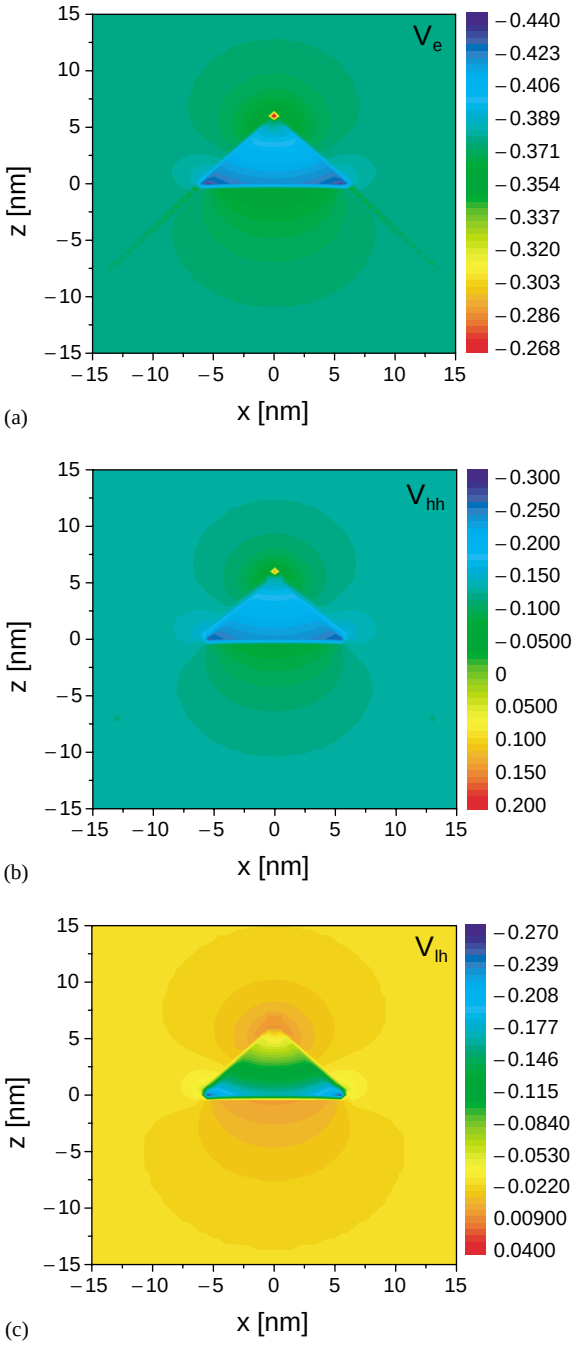

Fig. 12. Confining potential experienced by charge carriers in the x–z plane for structure PQD3 (negative values represent an attractive potential); (a) electrons, (b) heavy-holes, and (c) light-holes (potential expressed in eV).

the base. In the wetting layer, the potential is taken to be identical to the potential near to the base of the pyramid. The potential in the barrier is close to zero since the material here is GaAs. Fig. 12(b) shows the contour plot of the confining potential experienced by heavy-hole carriers. In the regions attractive to heavy-holes, the potential is negative. The potential inside the well has a positive gradient from the base towards the apex. Over this distance, the potential changes by several hundred meV. Because of this and the large effective mass for heavy-holes, one would expect charge localization near the base of the pyramid. The contour plot for the light-hole confining potential is shown in Fig. 12(c). This plot shows a slowly varying attractive potential in the barrier region above and below the pyramid. It reaches a minimum at the apex of the pyramid.

Several methods have been developed to calculate the electronic structure of the square-based pyramidal InAs dots [4,6,11]. Among these is the pseudopotential plane-wave approach used by Williamson et al. [32]. To calculate the energy levels and electron (or hole) wave functions we use an eight-band effective mass approach. The strain effect is included via deformation potential theory [33]. The bound energy levels are computed as functions of quantum-dot size. The bound states of the dot are found by numerically solving the Schrödinger equation, which in the effective mass approximation, can be written as

$$-\frac{\hbar^2}{2}\nabla\left(\frac{1}{m_i^*(r)}\right)\nabla\Psi_n(r)+V(r)\Psi_n(r) =E\Psi_n(r). \tag{23}$$

In this expression, $m_i^*(r)$ must be replaced by $m^*_{\mathrm{InGaAs}}(r)$ inside the dot, and by $m^*_{\mathrm{GaAs}}(r)$ in the matrix material; $V(r)$ is the three-dimensional confining potential. In the framework of the eight-band model, the wave function can be expanded as a linear combination of the basis functions, thus

$$\Psi_n(r)=\sum_{j=1}^{8}F_{nj}(r)u_j(r)=\sum_{J,J_z}|J,J_z\rangle F_{J,J_z}(r), \tag{24}$$

where $u_j(r)$ has the periodicity of the crystal lattice and j is the band index. At the band-edges, these functions are characterized by symmetry arguments as eigenstates $|J,J_z\rangle$ of the Bloch angular momentum J. The states $|J,J_z\rangle$ are the band-edge functions of the Bloch state space [34]. These wave functions are, for the s-like Γ_1 conduction band,

$$\left|\frac{1}{2},\frac{1}{2}\right\rangle_c=|S\rangle|\uparrow\rangle \quad\text{and}\quad \left|\frac{1}{2},-\frac{1}{2}\right\rangle_c=|S\rangle|\downarrow\rangle, \tag{25}$$

while for the p-like Γ_8, Γ_7 valence bands, they can be written as [34]

$$\begin{aligned}
\left|\frac{3}{2},\frac{3}{2}\right\rangle_{\mathrm{v}} &= \left(\frac{1}{\sqrt{2}}\right)(|x\rangle+i|y\rangle)|\uparrow\rangle,\\
\left|\frac{3}{2},\frac{1}{2}\right\rangle_{\mathrm{v}} &= \left(\frac{1}{\sqrt{6}}\right)(|x\rangle+i|y\rangle)|\downarrow\rangle - \left(\sqrt{\frac{2}{3}}\right)|z\rangle|\uparrow\rangle,\\
\left|\frac{3}{2},-\frac{1}{2}\right\rangle_{\mathrm{v}} &= -\left(\frac{1}{\sqrt{6}}\right)(|x\rangle-i|y\rangle)|\uparrow\rangle - \left(\sqrt{\frac{2}{3}}\right)|z\rangle|\downarrow\rangle,\\
\left|\frac{3}{2},-\frac{3}{2}\right\rangle_{\mathrm{v}} &= \left(\frac{1}{\sqrt{2}}\right)(|x\rangle-i|y\rangle)|\downarrow\rangle,\\
\left|\frac{1}{2},\frac{1}{2}\right\rangle_{\mathrm{v}} &= \left(\frac{1}{\sqrt{3}}\right)(|x\rangle+i|y\rangle)|\downarrow\rangle + \left(\sqrt{\frac{1}{3}}\right)|z\rangle|\uparrow\rangle,\\
\left|\frac{1}{2},-\frac{1}{2}\right\rangle_{\mathrm{v}} &= -\left(\frac{1}{\sqrt{3}}\right)(|x\rangle-i|y\rangle)|\uparrow\rangle + \left(\sqrt{\frac{1}{3}}\right)|z\rangle|\downarrow\rangle.
\end{aligned} \tag{26}$$

We want to point out that it is generally known that the $\boldsymbol{k}\cdot\boldsymbol{p}$ method has some problems associated with it when applied to calculations involving nanostructures [33]. These difficulties include (i) the fixed number of Bloch functions (eight in the formalism used here), (ii) the restriction of the validity of the method to the Brillouin zone center, (iii) the use of the same Bloch functions, regardless of material and strain variations,

and (iv) the difficulty of choosing appropriate boundary conditions with associated matching criteria for the envelope functions across the heterointerfaces. In our calculations, we take into account the variation of mass parameters from their bulk values due to the strain-induced band deformations. The details of the guidelines used have been discussed by Burt [35].

The eigenvalues and eigenfunctions of Eq. (23) are obtained by invoking periodic boundary conditions, expanding $\Psi_n(r)$ in terms of normalized plane-wave states, and diagonalizing the resulting matrix. This approach, which has also been used by Cusack et al. [6], does not require matching of the wave functions across the boundary between the dot and the matrix materials. This makes the method applicable to arbitrary (position dependent) confining potentials. The only requirement on the boundary conditions is that the states do not significantly overlap for dots adjacent to each other.

In general, the number of confined states in a quantum dot depends on the size of the dot and on the thickness of the wetting layer. For the conduction band, there are usually only a few bound states. The energy spacing between the ground state and the first excited state in the conduction band typically ranges from about 60 to 95 meV for the dot-sizes considered in our work (see Fig. 13). We find that the valence-band states are more tightly confined because of the large hole effective mass. The energy spacing here ranges from a few meV to 30 meV.

In our calculations, we have neglected the Coulomb interaction energy. This energy largely depends on the value of the dielectric constant. As a result, dots of the same size can belong to different confinement regimes in materials with different dielectric constants. In III–V compounds, with a typical relative dielectric constant of $\sim$13, the bulk exciton radius is >10 nm, causing a structural quantum dot of similar dimension and sufficiently deep potential to be in the strong confinement regime [22]. Because of this, additional binding energy from the Coulomb effect is negligible since the dots are already in the strong confinement regime. In any case, the Coulomb interaction energy is small compared to the separation of the ground state from the first excited state for both electrons and holes.

In Fig. 13, we show the calculated electron and hole energy level dependence on pyramid base length. The electron (hole) levels are plotted relative to the unstrained GaAs conduction (valence) band-edge. For dot base dimensions smaller than $\sim$6 nm, no bound electron states are predicted. Beyond 6 nm, a few states are predicted in the conduction band. And as stated earlier, many states are predicted in the valence band. This is due to the large effective mass associated with the holes and to the nature of the light-hole confining potential whose smoothly varying form leads to a quasi-continuum of tenuously bound states.

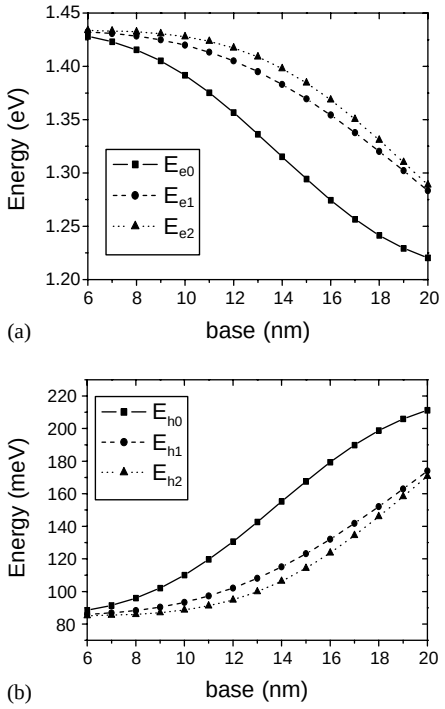

Fig. 13. (a) Electron and (b) hole quantum-dot energy levels (ground state and first two excited states), displayed as a function of dot base size.

We have also determined the envelope functions for the first few confined states in the dot. Fig. 14(a), for example, shows the modulus-squared envelope function for the E_{e0} state for structure PQD3; this function is plotted in the y–z plane, cutting through the pyramid and the wetting layer. The relatively isotropic character of the confining potential for electrons, coupled with the small effective mass, results in a state that permeates throughout the dot and penetrates into the sides of the pyramid. Fig. 14(b) is the hole envelope function in the y–z plane for the state E_{h0}. Unlike the ground state in the conduction band, the hole ground

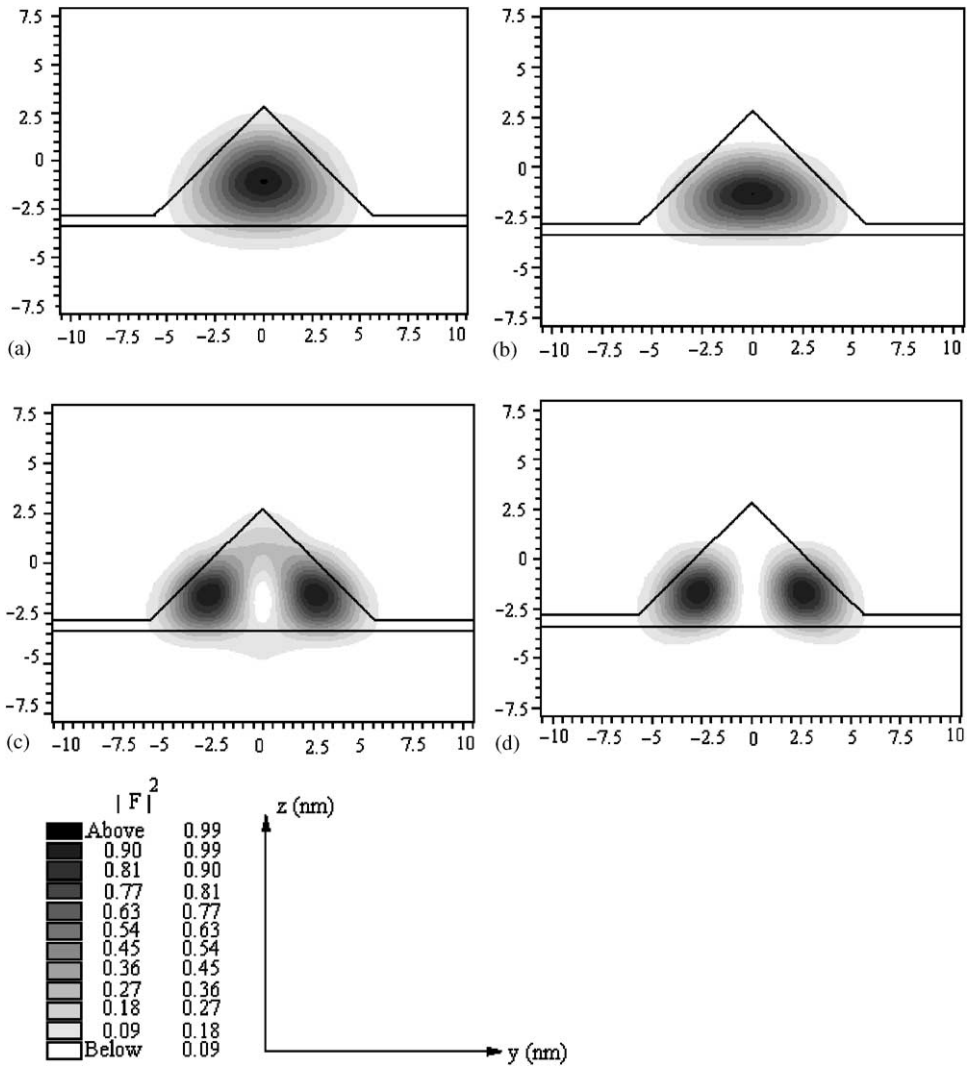

Fig. 14. The squared absolute magnitude of the envelope function for structure PQD3 across the y–z plane for energy levels: (a) E_{e0}, (b) E_{h0}, (c) E_{h1}, (d) E_{h2}.

state is confined to the base of the dot. In Fig. 14(c) and (d), we show the envelope functions for the hole excited states E_{h1} and E_{h2}.

The calculated transition energies for the ground state, $E_{e0} \rightarrow E_{h0}$, and for the first $E_{e1} \rightarrow E_{h1}$, and second $E_{e2} \rightarrow E_{h2}$ excited states for pyramids of various base dimensions are shown in Fig. 15(a). From Fig. 15(a), the calculated fundamental transition energy for a pyramid with a base length of 16 nm is 1.10 eV. This value is in good agreement with the experimentally determined transition peak at 1.098 eV shown in Fig. 15(b). The same good agreement is found between the calculated and measured peak luminescence energy values for a 20-nm-base pyramidal quantum dot; the measured experimental data is shown in Fig. 15(c).

The energy splitting between the ground state and first excited hole state of 30 meV in Fig. 15(b) is in good agreement with a recent experimental study of the sub-level structure which measured a difference

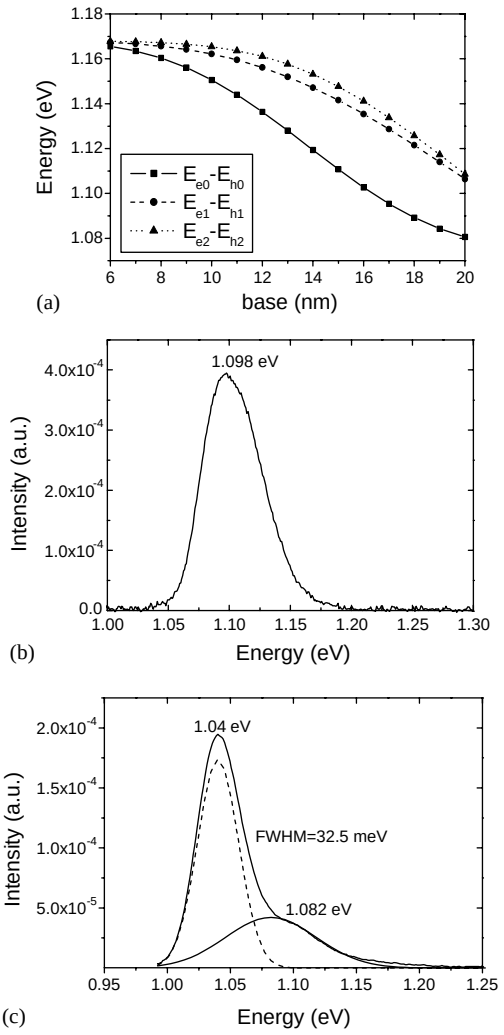

Fig. 15. (a) Calculated transition energies for pyramidal QDs: E_{e0}–E_{h0}, E_{e1}–E_{h1}, and E_{e2}–E_{h2}, as functions of QD base width; (b) Fundamental (E_{e0}–E_{h0}) transition energy measured by PL for a dot of base $B=16$ nm; and (c) for a dot of base width $B=20$ nm.

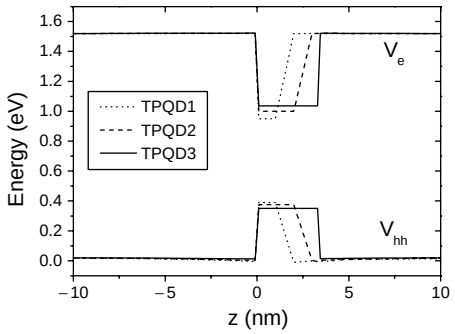

Fig. 16. Confining potentials for electrons and heavy-holes, along z-axis, for structures TPQD(1–3) with truncation factors: $t=0.25$ (TPQD1), $t=0.50$ (TPQD2), and $t=0.75$ (TPQD3).

of approximately 27 meV [36]. The $E_{e0} \rightarrow E_{h0}$ transition is the dominant excitation in all of the structures studied.

We now consider the computation of the electronic energy levels in truncated pyramidal quantum dots. The basic approach is similar to what has already been discussed in this paper. For truncation factors ranging from 0.25 to 0.75, we show the confining potentials for electrons and holes in Fig. 16. The bound states are determined by numerically solving the Schrödinger equation within the context of approximations similar to those used in the ideal pyramid case. The calculated energy levels for the ground state and two excited states in the conduction, as well as the valence bands are shown in Fig. 17 for a range of truncation factors. As a specific example, we calculated the energy levels for structure TPQD3, whose dimensions are given in Table 1; the TEM micrograph of this structure was shown in Fig. 8. The first three confined electron energy levels, measured with respect to the unstrained GaAs conduction band-edge, are $E_{e0}=1.404$ eV, $E_{e1}=1.426$ eV, and $E_{e2}=1.428$ eV. In the valence band, the corresponding heavy-hole levels—again measured with respect to the unstrained GaAs valence band-edge—are $E_{h0}=328.79$ meV, $E_{h1}=343.88$ meV, and $E_{h2}=345.74$ meV. The transition energies, for the allowed transitions, are shown in Fig. 18(a); the fundamental transition, $E_{e0} \rightarrow E_{h0}$, is at 1.076 eV. This energy is in good agreement with the experimentally determined peak of 1.08 eV for the photoluminescence emission spectrum shown in Fig. 18(b) for structure TPQD3. The photoluminescence measurements were carried out using an Ar^+ ion laser ($\lambda=488$ nm) as an excitation source. The emitted radiation was detected with a liquid-N_2-cooled Ge detector.

In devices such as near-infrared lasers and mid-infrared detectors, the preferred medium in the active region is often an (In,Ga)As/GaAs, rather than an InAs/GaAs quantum-dot superlattice. In this case, it becomes necessary to perform the energy level

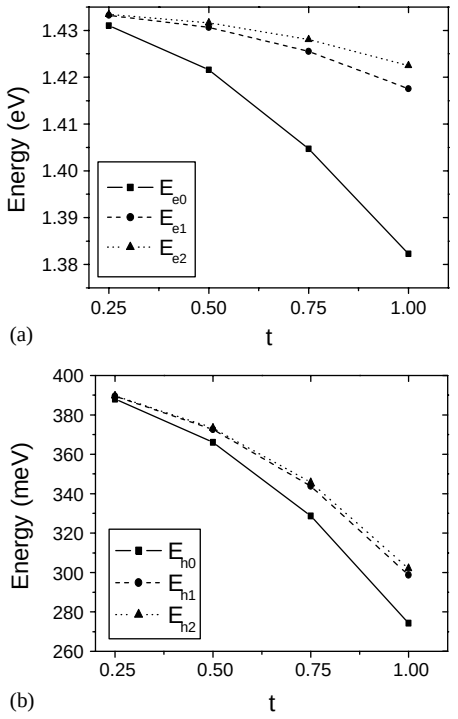

Fig. 17. Ground state and first two excited states for electrons and heavy-holes for structures TPQD(1–3) with truncation factors: $t = 0.25$–0.75.

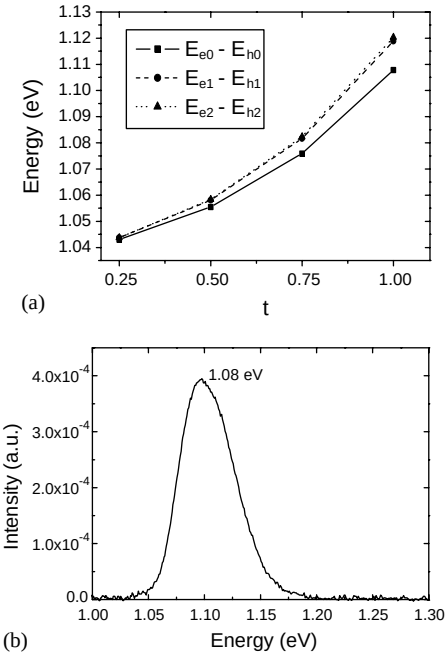

Fig. 18. Ground state and first excited state transition energies for structures TPQD(1–3) with truncation factors: $t = 0.25$–0.75: (a) calculated, (b) measured.

calculations for (In,Ga)As dots. We have performed such calculations for truncated pyramidal $In_{0.23}Ga_{0.77}As$ dots. The parameters used in the calculations are given in Table 2. For illustrative purposes, we have used the truncated structure TPQD4 in Table 1. The fundamental transition energy, $E_{e0} \rightarrow E_{h0}$, for such a structure is calculated to be 1.126 eV. In the conduction band, the electron ground state of such a dot is separated by about 107 meV from the first excited state. These computed values are in good agreement with the photoluminescence and infrared absorption data obtained at 300 K [37].

5. Conclusions

The relaxation of strain and its residual component in lattice-mismatched epitaxy is responsible for the self-organization of quantum dots in the Stranski–Krastanow crystal growth mode. Beginning from this premise, we have calculated the strain distributions in pyramidal and truncated pyramidal (In,Ga)As/GaAs quantum dots using a method based on Eshelby's inclusion theory of continuum elasticity. It is found that the hydrostatic component of the strain is mostly confined within the dots, while the biaxial strain is transferred from the dot to the barrier material. By taking into account the influence of the strain on the band gap of the dots, we have solved the three-dimensional, effective mass, single-particle Schrödinger equation for the electronic energy levels in the dot. We find that strain plays a major role in the energy structure of the quantum dots. For the pyramidal geometry considered here, the electronic energy levels are also a sensitive function of the base length.

The results of our calculations are in good agreement with those reported in the literature, even though our method is considerably simpler that those used by others [4,20]. For the fundamental transition of a ground state electron in the conduction band recombining with a hole in its ground state in the

valence band, we find that our experimental results also agree with calculations.

In summary, we have developed a simple method for rapidly calculating strain in embedded quantum dots. The method allows one to determine the interdependence of strain on shape, and by extension, the effects of strain on confined energy levels in quantum dots.

Acknowledgements

This work was supported by the Army Research Office, Research Triangle Park, NC, and by the Army Research Laboratory, Adelphi, MD.

Appendix A

This section gives the more general mathematical expressions for the stress distributions inside pyramidal InAs quantum dots of different degrees of truncation. The expressions are obtained by integrating Eq. (6). They are given as functions of the space coordinate z, in the growth direction. The strain components follow immediately from Hooke's law, as given in Eq. (15). The following definitions are used in the expressions: the pyramid base width is $B = 2a$; the height, in the absence of truncation, is H; the parameter t is the degree of truncation; and h is the height of a truncated pyramid. The stress component σ_{xx}, for example, is written as a summation over three terms:

$$\sigma_{xx} = \frac{h}{a^2+h^2}\,\frac{E\varepsilon_0}{4\pi(1-\nu)} \times[\sigma'_{xx(1)} + \sigma'_{xx(2)} + \sigma'_{xx(3)}], \tag{A.1}$$

where the terms $\sigma'_{xx(1)}$, $\sigma'_{xx(2)}$, and $\sigma'_{xx(3)}$ are given as

$$\sigma'_{xx(1)} = \frac{4a^2}{\sqrt{2a^2+h^2}}\left\{\ln\left[\frac{-2a^2(1-t)-h(z-ht)}{\sqrt{2a^2+h^2}} + \sqrt{2a^2(1-t)^2+(z-ht)^2}\right] - \ln\left[\frac{-2a^2-hz}{\sqrt{2a^2+h^2}} + \sqrt{2a^2+z^2}\right]\right\}. \tag{A.2}$$

$$\sigma'_{xx(2)} = 2h\left\{\tan^{-1}\left[\frac{-(z-ht)}{\sqrt{2a^2(1-t)^2+(z-ht)^2}}\right] - \tan^{-1}\left[\frac{(z-ht)}{\sqrt{2a^2(1-t)^2+(z-ht)^2}}\right] + \tan^{-1}\left[\frac{z}{\sqrt{2a^2+z^2}}\right] - \tan^{-1}\left[\frac{-z}{\sqrt{2a^2+z^2}}\right]\right\}, \tag{A.3}$$

and

$$\sigma'_{xx(3)} = a\ln\left\{[a(1-t)+\sqrt{2a^2(1-t)^2+(z-ht)^2}] \times\left[2a^2\left(1-\frac{z}{h}\right)^2 - a + \sqrt{2a^2+z^2}\right] \times 2a^2\left(1-\frac{z}{h}\right)^2(-a+\sqrt{2a^2+z^2})\right\} - a\ln\left\{[-a(1-t)+\sqrt{2a^2(1-t)^2+(z-ht)^2}] \times\left[2a^2\left(1-\frac{z}{h}\right)^2 + a + \sqrt{2a^2+z^2}\right] \times 2a^2\left(1-\frac{z}{h}\right)^2(a+\sqrt{2a^2+z^2})\right\}. \tag{A.4}$$

Similarly, for σ_{yy} we derive the following relations along the z-axis:

$$\sigma_{yy} = \frac{h}{a^2+h^2}\,\frac{E\varepsilon_0}{4\pi(1-\nu)}[\sigma'_{yy(1)} + \sigma'_{yy(2)} + \sigma'_{yy(3)}], \tag{A.5}$$

with $\sigma'_{yy(1)}$, $\sigma'_{yy(2)}$, and $\sigma'_{yy(3)}$ given as

$$\sigma'_{yy(1)} = \frac{4a^2}{\sqrt{2a^2+h^2}}\left\{\ln\left[\frac{-2a^2(1-t)-h(z-ht)}{\sqrt{2a^2+h^2}} + \sqrt{2a^2(1-t)^2+(z-ht)^2}\right] - \ln\left[\frac{-2a^2-hz}{\sqrt{2a^2+h^2}} + \sqrt{2a^2+z^2}\right]\right\}, \tag{A.6}$$

$$\sigma'_{yy(2)} = 2h\left\{\tan^{-1}\left[\frac{-(z-ht)}{\sqrt{2a^2(1-t)^2+(z-ht)^2}}\right] -\tan^{-1}\left[\frac{(z-ht)}{\sqrt{2a^2(1-t)^2+(z-ht)^2}}\right] +\tan^{-1}\left[\frac{z}{\sqrt{2a^2+z^2}}\right]-\tan^{-1}\left[\frac{-z}{\sqrt{2a^2+z^2}}\right]\right\}, \tag{A.7}$$

$$\sigma'_{yy(3)} = a\ln\left\{[a(1-t)+\sqrt{2a^2(1-t)^2+(z-ht)^2}] \times\left[2a^2\left(1-\frac{z}{h}\right)^2-a+\sqrt{2a^2+z^2}\right] \times 2a^2\left(1-\frac{z}{h}\right)^2(-a+\sqrt{2a^2+z^2})\right\} - a\ln\left\{[-a(1-t)+\sqrt{2a^2(1-t)^2+(z-ht)^2}] \times\left[2a^2\left(1-\frac{z}{h}\right)^2+a+\sqrt{2a^2+z^2}\right] \times 2a^2\left(1-\frac{z}{h}\right)^2(a+\sqrt{2a^2+z^2})\right\}. \tag{A.8}$$

The other stress component, σ_{zz}, follows from:

$$\sigma_{zz} = \frac{2E\varepsilon_0}{(1-v)} - (\sigma_{xx}+\sigma_{yy}). \tag{A.9}$$

References

[1] A. Harvey, H. Davock, A. Dunbar, U. Bangert, P.J. Goodhew, J. Phys. D: Appl. Phys. 34 (2001) 636.
[2] D. Leonard, K. Pond, P.M. Petroff, Phys. Rev. B 50 (1994) 11 689.
[3] E.P. O'Reilly, Semicond. Sci. Technol. 4 (1989) 121.
[4] M. Grundmann, O. Stier, D. Bimberg, Phys. Rev. B 52 (1995) 11 969.
[5] T. Benabbas, P. François, Y. Androussi, A. Lefebre, J. Appl. Phys. 80 (1996) 2763.
[6] M.A. Cusack, P.R. Briddon, M. Jaros, Phys. Rev. B 54 (1996) R2300.
[7] Y. Kikuchi, H. Sugii, K. Shintani, J. Appl. Phys. 89 (2001) 1191.
[8] S. Christiansen, M. Albrecht, H.P. Strunk, H.J. Maier, Appl. Phys. Lett. 64 (1994) 3617.
[9] L. De Caro, L. Tapfer, Phys. Rev. B 49 (1994) 11 127.
[10] D.A. Faux, S.G. Howells, U. Bangert, A.J. Harvey, Appl. Phys. Lett. 64 (1994) 1271.
[11] A.H. Harker, K. Pinardi, S.C. Jain, A. Atkinson, R. Bullough, Philos. Mag. A 71 (1995) 871.
[12] P.K. Banerjee, Boundary Element Methods in Engineering, Mc.Graw-Hill, London, 1994.
[13] J.R. Downes, D.A. Faux, E.P. O'Reilly, J. Appl. Phys. 81 (1997) 6700.
[14] J.D. Eshelby, Proc. R. Soc. London Ser. A 241 (1957) 376.
[15] T. Benabbas, Y. Androussi, A. Lefebre, J. Appl. Phys. 86 (1999) 1945.
[16] A.D. Andreev, J.R. Downes, D.A. Faux, E.P. O'Reilly, J. Appl. Phys. 86 (1999) 297.
[17] O. Brandt, K. Ploog, R. Bierwolf, M. Hosenstein, Phys. Rev. Lett. 68 (1992) 1339.
[18] D.A. Faux, G. Jones, E.P. O'Reilly, Modell. Simul. Mat. Sci. Eng. 2 (1994) 9.
[19] D.A. Faux, J. Haigh, J. Phys.: Condens. Mater 2 (1990) 10 289.
[20] C. Pryor, J. Kim, L.W. Wang, J. Williamson, A. Zunger, J. Appl. Phys. 83 (1998) 2548.
[21] J. Kim, L.W. Wang, A. Zunger, Phys. Rev. B 57 (1998) R9408.
[22] D. Bimberg, M. Grundmann, N.N. Ledentsov, Quantum Dot Heterostructures, Wiley, UK, 1998.
[23] A.S. Saada, Elasticity: Theory and Applications, Pergamon Press, New York, 1974.
[24] C. Pryor, Phys. Rev. B 57 (1998) 7190.
[25] P. Sutter, M.G. Lagally, Phys. Rev. Lett. 81 (1998) 3471.
[26] J. Demarest, Ph.D. Dissertation, University of Virginia, 2001, p. 172.
[27] K. Muraki, S. Kukatsu, Y. Shirali, R. Ito, Appl. Phys. Lett. 61 (1992) 557.
[28] C. Lanczos, J. Res. Nat. Bur. Stand. 45 (1950) 255.
[29] J.K. Cullum, R.A. Willoughby, Lanczos Algorithms for Large Symmetric Eigenvalue Computations, Birkhauser, Boston, 1985.
[30] C.G. Van der Walle, Phys. Rev. B 39 (1989) 1871.
[31] G. Cipriani, M. Rosa-Clot, S. Taddei, Phys. Rev. B 61 (2000) 7536.
[32] A.J. Williamson, A. Zunger, Phys. Rev. B 59 (1999) 15 819.
[33] O. Stier, M. Grundmann, D. Bimberg, Phys. Rev. B 59 (1999) 5688.
[34] F.H. Pollak, Semicond. Semimet. 32 (1990) 17.
[35] M.G. Burt, J. Phys.: Condens. Matter 4 (1992) 6651.
[36] K.H. Schmidt, G. Medeiros-Ribeiro, M. Oestreich, G.H. Döhler, P.M. Petroff, Phys. Rev. B 54 (1996) 11 346.
[37] D. Pal, V.G. Stoleru, E. Towe, Jpn. J. Appl. Phys. 41 (1) (2001) 482.
[38] C. Pryor, Phys. Rev. B 60 (1999) 2869.
[39] S.L. Chuang, Physics of Optoelectronic Devices, Wiley, New York, 1995.
[40] K.H. Hellwege, in: Landolt-Börnstein (Ed.), Numerical Data and Functional Relationships in Science and Technology, New Series, Group III 17a, Springer, Berlin, 1982; Groups III–V 22a, Springer, Berlin, 1986.